Doped ordered mesoporous carbons as novel, selective electrocatalysts for the reduction of nitrobenzene to aniline

Daems, Nick; Risplendi, Francesca; Baert, Kitty; Hubin, Annick; Vankelecom, Ivo F. J.; Cicero, Giancarlo; Pescarmona, Paolo P.

Published in:
Journal of Materials Chemistry A

DOI:
10.1039/C8TA01609G

Journal of Materials Chemistry A

PAPER

View Article Online
View Journal | View Issue

Cite this: J. Mater. Chem. A, 2018, 6, 13397

Doped ordered mesoporous carbons as novel, selective electrocatalysts for the reduction of nitrobenzene to aniline†

Nick Daems,[ab] Francesca Risplendi,[c] Kitty Baert,[d] Annick Hubin,[d] Ivo F. J. Vankelecom,[a] Giancarlo Cicero[c] and Paolo P. Pescarmona[*e]

Ordered mesoporous carbons (OMCs) doped with nitrogen, phosphorus or boron were synthesised through a two-step nanocasting method and studied as electrocatalysts for the reduction of nitrobenzene to aniline in a half-cell setup. The nature of the dopant played a crucial role in the electrocatalytic performance of the doped OMCs, which was monitored by LSV with a rotating disk electrode setup. The incorporation of boron generated the electrocatalysts with the highest kinetic current density, whereas the incorporation of phosphorus led to the lowest overpotential. Doping with nitrogen led to intermediate behaviour in terms of onset potential and kinetic current density, but provided the highest selectivity towards aniline, thus resulting in the most promising electrocatalyst developed in this study. Density functional theory calculations allowed explaining the observed difference in the onset potentials between the various doped OMCs, and indicated that both graphitic N and pyrdinic N can generate active sites in the N-doped electrocatalyst. A chronoamperometric experiment over N-doped OMC performed at −0.75 V *vs.* Fc/Fc^+ in an acidic environment, resulted in a conversion of 61% with an overall selectivity of 87% to aniline. These are the highest activity and selectivity ever reported for an electrocatalyst for the reduction of nitrobenzene to aniline, making N-doped OMC a promising candidate for the electrochemical cogeneration of this industrially relevant product and electricity in a fuel cell setup.

Received 15th February 2018
Accepted 14th June 2018

DOI: 10.1039/c8ta01609g

rsc.li/materials-a

1. Introduction

Nowadays, the fuel cell industry and the chemical industry run mainly independently from each other. This means that fuel cells are almost exclusively used for the generation of electricity, with water or carbon dioxide as end product. However, since many industrially valuable chemicals can be obtained by means of thermodynamically favourable redox reactions ($\Delta_r G^\circ < 0$), the prospect exists of carrying out these syntheses in a fuel cell setup. This approach has the advantage that the chemical energy liberated by the reaction, which is typically lost as heat in the current process, is converted into electricity. In this way, the production of industrially valuable products could be coupled with the generation of electricity. This cogeneration approach would lead to more sustainable and energy-efficient processes, which is in line with the current societal and industrial targets.[1–3] An additional advantage of an electrochemical over a conventional production process, is the possibility to control the selectivity and the reaction rate through the cell potential.[4,5]

While this is a relatively new and yet largely unexplored field, several examples do exist in literature. Amongst others, they include the reduction of oxygen to hydrogen peroxide,[2,6–9] the reduction of nitrogen monoxide to hydroxylamine,[4,5,10,11] the reduction of nitrobenzene to aniline[1,12–15] and the oxidation of glycerol.[16–20] This study focuses on the reduction of nitrobenzene to aniline, which is a compound with a broad range of industrial applications,[21] among which the most important is as intermediate in the production of polyurethanes.[22]

The electrochemical reduction of the nitro group was first investigated by Haber and Schmidt and has been extensively studied since then.[1,12,13,23,24] The overall reactions are:

$$\text{Anode: } H_2 \rightarrow 2H^+ + 2e^-,\ E^\circ = 0\ \text{V} \quad (1)$$

$$\text{Cathode: } PhNO_2 + 6H^+ + 6e^- \rightarrow PhNH_2 + 2H_2O,\ E^\circ = 0.82\ \text{V} \quad (2)$$

[a]Centre for Surface Chemistry and Catalysis, KU Leuven, Celestijnenlaan 200F, 3001 Heverlee, Belgium
[b]Advanced Reactor Technology, U Antwerpen, Campus Drie Eiken, Universiteitsplein 1 2610 Wilrijk, Belgium
[c]Applied Science and Technology Department, Politecnico di Torino, Corso Duca degli Abruzzi 24, 10129 Torino, Italy
[d]Research Group Electrochemical and Surface Engineering, Vrije Universiteit Brussel, Pleinlaan 2, 1050 Brussels, Belgium
[e]Chemical Engineering Group, Engineering and Technology Institute Groningen (ENTEG), University of Groningen, Nijenborgh 4, 9749 AG Groningen, The Netherlands. E-mail: p.p.pescarmona@rug.nl

† Electronic supplementary information (ESI) available. See DOI: 10.1039/c8ta01609g

As discussed in detail elsewhere,[13] the full reaction scheme is more complex and contains several reaction intermediates and side-products, which originate from both electrochemical and chemical steps (Scheme 1).[25] Importantly, the product selectivity and the reaction rate is strongly influenced by the physico-chemical features of the electrocatalyst employed at the cathode.[1,14,26–32] In order to make this electrochemical route towards aniline economically viable, it is of utmost importance to develop cost-effective and productive electrocatalysts with a high selectivity towards the target product, aniline. Recent research performed by our group has shown that Cu nanoparticles supported on multi-walled carbon nanotubes (MWCNTs) outperformed their Pt counterparts in terms of onset potential, proving the possibility to use non-noble metals as less expensive catalytic species.[1,12,13] Further investigation of electrocatalysts containing non-noble metals (Fe, Co and Cu) supported on N-doped carbon led to the identification of an electrocatalyst with a low loading of highly dispersed Cu_xO/Cu species with much enhanced selectivity towards the desired aniline product.[33] This study also suggested that non-metallic sites could play a catalytic role, in analogy to recent results obtained on N-doped diamond.[32] Therefore, and in an attempt to further reduce the electrocatalyst cost, the possibility to use ordered mesoporous carbons (OMCs) doped with nitrogen, boron or phosphorus as electrocatalysts for the nitrobenzene reduction is investigated in this work. Doped carbon materials were chosen since they consist of inexpensive, widely available elements and are devoid of metals. Furthermore, the presence of a graphitic carbon backbone grants a high electrochemical stability and a good electron conductivity.[34,35] Doping the graphitic carbon framework disrupts the electron delocalisation in the graphitic π-system, generating sites with pairs of partial positive and negative charges, which may act as active sites for the nitrobenzene reduction (easier adsorption of the negatively charged oxygen atom of the nitro-group on the positive sites).[34] There are several reasons why doped OMCs were targeted over doped carbon nanotubes or doped graphene. First of all, they possess a higher specific surface area (up to 1900 $m^2 g^{-1}$), which is anticipated to result in a higher number of accessible active sites.[36,37] Furthermore, the presence of mesopores grants easier accessibility of the active sites compared to microporous materials.[34,38] Finally, since they can be prepared in the absence of metals, they are virtually metal-free, which is not necessarily the case with graphene or carbon nanotubes.[39–42] While doped OMCs have been extensively studied for the oxygen reduction reaction (showing promising results),[2,34,36,38,43,44] they have not yet been applied for the electrochemical reduction of nitrobenzene to aniline. In this work, a two-step nanocasting method previously developed by our group to prepare N-doped OMC,[2] was modified to synthesise OMCs doped also with boron or phosphorus. This synthesis method offers several advantages. First, by using SBA-15 silica with its interconnected two-dimensional mesoporous structure as hard template, doped OMCs with high specific surface area can be obtained. Secondly, by covering the template pore walls first with a dopant precursor, a high accessibility of the active sites can be ensured. Finally, compared to the technique that is required to prepare N-doped diamond, this synthesis method requires less severe conditions and is less expensive.[34] The synthesised doped OMC materials were thoroughly characterised and tested for the first time as electrocatalysts for the reduction of nitrobenzene, displaying the highest selectivity reported so far towards the target aniline product. In addition, Density Functional Theory (DFT) calculations highlighted the fundamental role of the heteroatom doping site on the catalytic activity of the doped OMC materials.

2. Experimental and computational methods

2.1 Materials

The following chemicals were used in this work: aniline (99.8%, pure, Acros Organics), dihydroxynaphthalene (≥98%, Sigma

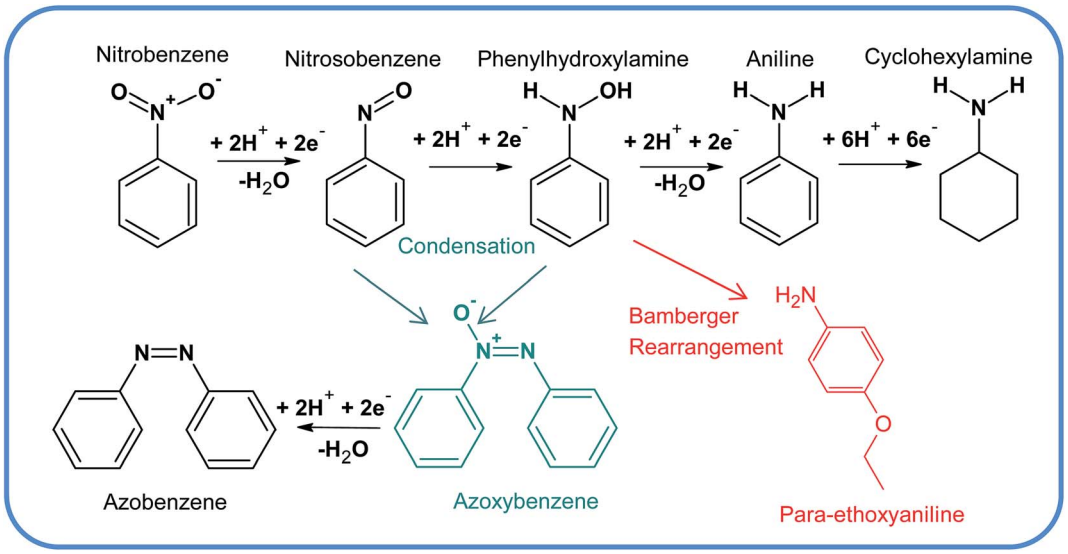

Scheme 1 Main and side reaction paths in the electrochemical reduction of nitrobenzene.

Aldrich), Pluronic P123 (Sigma Aldrich), tetraethyl orthosilicate (Sigma Aldrich, reagent grade), glycerol (>99.5%, Sigma Aldrich), benzene-1,4-diboronic acid (≥95%, Sigma Aldrich), tris(4-methoxyphenyl)phosphine (98%, Alfa Aesar), ammonium peroxydisulfate (98%, Acros Organics), sulphuric acid (>95%, Fisher Chemical), hydrochloric acid (37% aqueous solution, Fisher Chemical), perchloric acid (70% aqueous solution, Sigma Aldrich), nitrobenzene (≥99%, Sigma Aldrich) and phosphate buffer (pH = 7, Fisher). All these chemicals were used as received from commercial sources.

2.2 Synthesis of the electrocatalysts

Doped ordered mesoporous carbon materials were prepared through methods inspired by a procedure previously developed by our group (Scheme 2).[2] Briefly: in the first step, the SBA-15 hard template was synthesised, calcined and then 0.5 g of it ($S_{BET} = 819\ m^2\ g^{-1}$ and $V_{pores} = 0.66\ cm^3\ g^{-1}$) was impregnated with the dopant precursor. Three different dopant precursors were used: one N-containing, *i.e.* aniline (NOMC); one P-containing, *i.e.* tris(4-methoxyphenyl)phosphine (POMC); and one B-containing, *i.e.* benzene-1,4-diboronic acid (BOMC). In each case, the amount of dopant precursor to be employed was determined as the amount estimated to be necessary to cover the SBA-15 surface with a monolayer, based on the molecular cross-sectional area of each precursor.[2] The calculated amounts were then gradually adapted by increasing the amount of precursor (if the pores were not completely filled) or by decreasing it (if unordered material was observed by TEM besides the desired ordered structure). This optimisation led to the following final amounts: 0.17 g for aniline, 0.24 g for tris(4-methoxyphenyl)phosphine and 0.30 g for benzene-1,4-diboronic acid. For the synthesis of NOMC, aniline and 0.5 g of ammonium peroxydisulfate (employed to initiate the aniline polymerisation) were added to 250 ml of a suspension of 0.5 g of SBA-15 in 0.5 M aqueous HCl and stirred for 24 h at $0 < T < 4$ °C. For the synthesis of BOMC and POMC, the respective precursors were added to 10 ml of a suspension of 0.5 g of SBA-15 in acetone and stirred for 24 h at RT. After evaporation of the solvent, each material was pyrolysed for a first time at 900 °C for 3 h under N_2 flow ($1\ cm^3\ s^{-1}$). Next, the remaining pore volume was filled up with dihydroxynaphthalene (0.20 g, 0.12 g and 0.13 g for the N-doped, P-doped and B-doped OMCs, respectively), followed by a second pyrolysis at 900 °C for 3 h under N_2 flow ($1\ cm^3\ s^{-1}$). Finally, the SBA-15 template was removed by treatment with a NaOH solution (2.5 wt% in a 50/50 water/ethanol mixture). For a more detailed description we refer to our previous work on N-doped ordered mesoporous carbon materials.[2] As a reference and to investigate the influence of oxygen species, a material was synthesised using only dihydroxynaphthalene (0.44 g) to fill up the complete pore volume (OMC). The materials are further referred to using their respective abbreviations, *i.e.* OMC, BOMC, NOMC and POMC (see Scheme 2). Prior to physicochemical and/or electrochemical characterisation, the samples were stored under N_2 in a desiccator.

2.3 Physicochemical characterisation

Nitrogen adsorption–desorption isotherms were measured at 77 K on a Micromeritics Tristar 3000 after a pretreatment at 300 °C for 5 h under N_2 atmosphere to remove residual water. The pore size distributions were determined using the Barrett–Joyner–Halenda (BJH) method, whereas the Brunauer–Emmett–Teller (BET) method was used to calculate the specific surface area of the samples. Transmission electron microscopy (TEM) images were taken at MTM-KU Leuven, using a Philips FEG CM200 operated at 200 kV. Samples were prepared by dispersing the

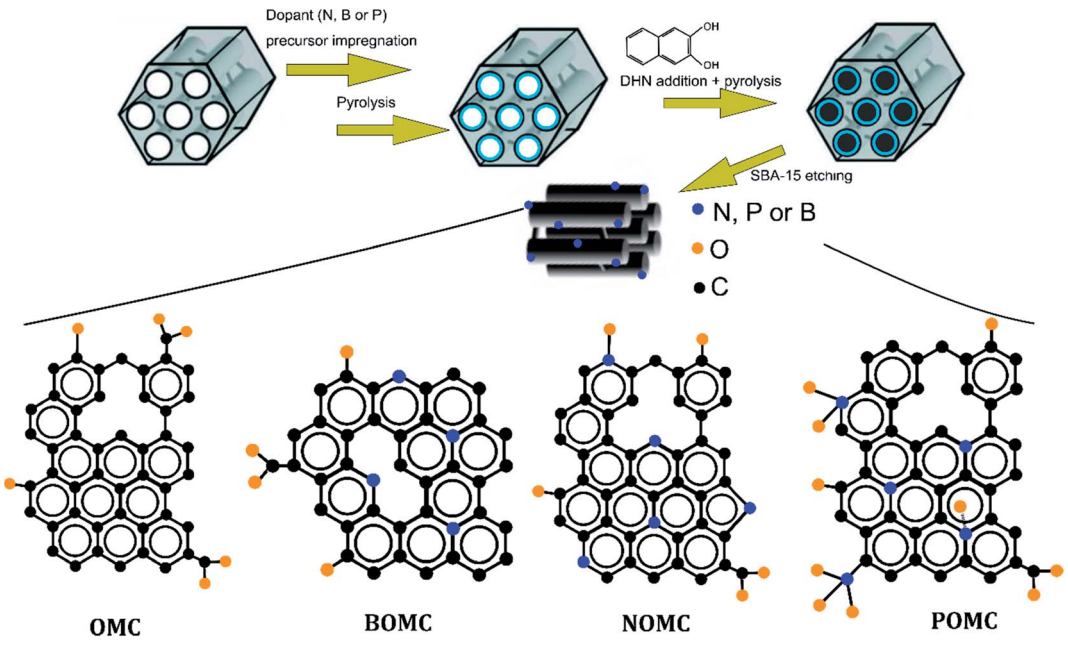

Scheme 2 Synthesis route for preparing the doped ordered mesoporous carbon materials.

powders in ethanol and placing several drops of the dispersion onto a holey carbon grid. X-ray photoelectron spectroscopy (XPS) measurements were carried out on a Physical Electronics PHI 1600 multi-technique system using an Al Kα (1486.6 eV) monochromatic X-ray source operated at 15 kV and 150 W at a base pressure of 2×10^{-9} torr. The graphitic C 1s band at 284.6 eV was used as internal standard, in order to correct possible deviations caused by electric charging of the samples. The MultiPak software was employed for the deconvolution and integration of the XPS signals using Gaussian curves for fitting. Room-temperature Raman spectra were measured on a LabRAM HR Evolution spectrometer from HORIBA Scientific. The spectrometer was equipped with a high stability confocal microscope with XYZ motorised stage and objectives for 10×, 50×, 100× magnification, a multichannel air cooled detector (with a spectral resolution of <1 cm^{-1}) and a solid state laser at a wavelength of 532 nm (Nd : YAG). Deconvolution and peak integration was carried out by means of the Igor pro software. X-ray fluorescence (XRF) spectra were measured on a Bruker S8 Tiger, equipped with a 4 kW rhodium X-ray tube. The samples were measured using the QuantExpress semi-quantitative method. This method employs three different crystals (PET, XS-55, Lif200) to divide the fluorescence spectrum originating from the sample into the specific wavelengths of the elements. Two detectors were employed: a proportional counter for light elements and a scintillation counter for the heavy elements. The samples were measured in a plastic holder with a bottom consisting of Mylar foil.

2.4 Electrochemical characterisation

All electrochemical measurements were performed in a half cell setup using a Gamry Interface 1000E potentiostat, using glassy carbon porous rotating disk electrodes (d = 5 mm). The electrocatalysts were deposited as an ink on the surface of these electrodes. For each measurement, the ink was prepared by dispersing 24.0 mg of electrocatalyst in 900 μl of a 1 wt% solution of polystyrene in toluene. Approximately 3.47 μl of this ink was deposited on the glassy carbon electrode, after which toluene was evaporated at 50 °C for 20 min in a vacuum oven. This procedure resulted in an average catalyst loading of 0.47 mg cm^{-2}. While this might result in a relatively thick active layer, it is expected that the accessibility to the active sites is granted by the mesoporous nature of the applied electrocatalyst.[44] The reference electrode was a Fc/Fc^+ reference electrode system ($E^\circ_{Fc/Fc+}$ = 0.64 V *vs.* S.H.E.) and the counter electrode was a Pt grid. All potentials are referred to the Fc/Fc^+ redox couple. The linear sweep voltammetry (LSV) measurements were carried out in 0.3 M $HClO_4$ in ethanol. To avoid possible interference of the oxygen reduction reaction, N_2 was bubbled through the electrolyte for at least 30 min to remove O_2 prior to the measurements. The electrolyte temperature was kept at 25 °C with a thermostatic bath. For the LSV measurements, 50 ml of 5 mM nitrobenzene electrolyte solution was used. The potential was scanned in the range from −0.2 to −1.8 V *vs.* Fc/Fc^+ at a rate of 5 mV s^{-1}. For each electrocatalyst, blank measurements, *i.e.* in absence of nitrobenzene, were recorded before investigating the nitrobenzene reduction. The reliability of the experimental results was granted by repeating each measurement at least two times and by reporting the average values. The potential of each measurement was corrected for the ohmic potential drop (equal to 125 ohm, as determined by electrochemical impedance spectroscopy) as a consequence of the electrolyte resistance between the reference and the working electrode.

The onset potential, *i.e.* the potential at which the nitrobenzene reduction reaction starts, was determined as the potential at which the slope of the LSV plot exceeded 0.1 mA cm^{-2} V^{-1}. The half-wave potential ($E_{1/2}$), *i.e.* the potential at which the reaction is in the middle of the mixed kinetic-diffusion regime, was determined as the potential corresponding to the inflection point in the LSV plot. The Koutécky–Levich (K–L) equation (eqn (3)) was used to calculate the number of exchanged electrons (n) and to determine the kinetic current density:[38]

$$\frac{1}{J} = \frac{1}{J_K} + \frac{1}{J_D} = \frac{1}{nFkC_0} + \frac{1}{0.62nFC_0{D_0}^{2/3}\nu^{-1/6}\omega^{1/2}} \quad (3)$$

where J is the recorded current density, which consists of a kinetic factor (J_K) and a diffusion-limited current density (J_D), n is the number of transferred electrons, F is the Faraday constant, k is the electron transfer rate constant, C_0 is the concentration of nitrobenzene in the bulk (5×10^{-6} mol cm^{-3}), ν is the kinematic viscosity of the electrolyte (0.0152 cm^2 s^{-1}), D_0 is the diffusion coefficient (4.7×10^{-6} cm^2 s^{-1}) and ω is the rotation speed of the rotating disk electrode.[12] At a chosen potential, n can be determined from the slope of the K–L plots. The kinetic current density can be determined from the intercept with the y-axis. The current densities were calculated with respect to the geometric surface area of the glassy carbon electrode (A_{geo} = 0.20 cm^2) since it is not possible to accurately determine the actual surface area, which depends both on the specific surface area of the electrocatalyst and on the amount of binder and electrocatalyst that are applied on the disk. Therefore, the kinetic current densities reported in this work include contribution of both the intrinsic activity (per surface unit) and of the specific surface area of the electrocatalyst.[13] This allows a meaningful comparison of the electrocatalytic performance of different materials. However, it should be realised that this ranking differs from reports where the electrochemically active surface area is used to normalise the kinetic current density, in which case the kinetic current density is a direct measure of the intrinsic activity (per surface unit).

In order to investigate the conversion and the product selectivity in the nitrobenzene reduction reaction over the most promising electrocatalysts, chronoamperometric experiments were performed in a single cell in which the two half cells are separated by means of a Zirfon® membrane.[45] The rotation speed of the working electrode was set at 500 rpm and the potential was set at −0.75 V *vs.* Fc/Fc^+ in 0.3 M $HClO_4$ in ethanol. The volume of the half cell with the working electrode was 170 ml and a concentration of 15 mM of nitrobenzene was used. After 52 h, the pH of the reaction solution was adjusted to 7 with a 1 M KOH ethanolic solution and a phosphate buffer

solution,[33] and insoluble $KClO_4$ was filtered out. Analysis of the products after chronoamperometry was performed using gas chromatography (GC) on a Shimadzu 2010 Plus equipped with a Rtx-5 amine-functionalised standard capillary column (15 m, 0.25 mm internal diameter). Each GC analysis was done in triplicate and the average results were reported. The conversion was calculated based on the GC data and compared to the conversion values calculated with Faraday's law:

$$n_{\text{reacted}} = \frac{Q}{Fn} \quad (4)$$

where n_{reacted} is the number of moles of nitrobenzene that reacted, Q is the amount of charge that passed through the system (measured using the area under the chronoamperometry curve), F is the Faraday constant and n is the average number of exchanged electrons per molecule of nitrobenzene. The conversion can be calculated by dividing n_{reacted} by the initial number of moles of nitrobenzene.

Cyclic voltammetry (CV) was used to evaluate the electrochemical stability of selected electrocatalysts. The potential was cycled at a scan rate of 100 mV s^{-1} between −0.2 to −1.8 V *vs.* Fc/Fc^+ in a half-cell containing 5 mM nitrobenzene in a 0.3 M $HClO_4$ ethanolic solution. 1000 cycles were performed. Prior to the last scan the solution was stirred to get a homogeneous nitrobenzene distribution. The second and the last scan were compared to evaluate the electrocatalyst stability.

2.5 Computational approach

The theoretical calculations were based on the Density Functional Theory (DFT) as implemented in the Quantum Espresso package.[46] The Kohn–Sham (KS) equations were solved using ultrasoft pseudopotential to describe the electron-ion interaction, employing the gradient corrected Perdew–Burke–Ernzerhof (PBE) functional[47] to describe the exchange–correlation effects, and expanding the electronic wave functions in plane waves (PW). Dispersion interactions were taken into account by employing the DFT-D2 method.[48,49] For all calculations, a PW energy cut-off of 28 Ry was adopted for the wave functions and of 280 Ry for the charge density and potentials. Both 4 × 4 and 6 × 6 graphene supercells were employed to simulate the surface of the B-, P- or N-doped OMCs and the adsorption of nitrobenzene. A vacuum of 10 Å thickness was added in the direction perpendicular to the 2D layers to avoid spurious interaction between periodic replicas. The Brillouin Zone (BZ) was sampled employing a 12 × 12 × 1 Monkhorst–Pack mesh[50] or reduced grid in case of supercells, to maintain consistent k-points density. All structures were relaxed by minimising the atomic forces; convergence was assumed when the maximum component of the residual forces on the ions was smaller than 10^{-4} Ry per bohr. The adsorption energy (ΔE_{ads}) of the nitrobenzene molecule on pure and doped graphene was evaluated by calculating $\Delta E_{\text{ads}} = E_{\text{tot}} - E_{\text{mat}} - E_{\text{mol}}$, where E_{tot} is the total energy of the system formed by a molecule adsorbed on the surface of the material (after optimisation of the geometry of the system), and E_{mat} and E_{mol} correspond to the total energy of the relaxed material and isolated molecule, respectively.

3 Results and discussion

Ordered mesoporous carbons doped with different elements (N, B, or P) were prepared by modifying a two-step nanocasting method that was developed by our group.[2] It is the first time that this type of electrocatalysts was tested for the electrocatalytic reduction of nitrobenzene, with the industrially relevant aniline as target product. The electrocatalysts were ranked based on product selectivity (number of exchanged e^-) and activity (onset potential and kinetic current density). The electrocatalyst performance was correlated to the physicochemical properties determined through a combination of experimental and simulation techniques in order to understand which features of the materials led to the most efficient electrocatalyst for the reduction of nitrobenzene to aniline.

The success of the applied synthesis strategy in preparing OMCs with a high specific surface area and with nitrogen-, boron- or phosphorus-doping in the graphitic carbon framework was demonstrated by TEM, N_2 physisorption and XPS. TEM was used to investigate the pore structure of the different materials (Fig. 1). The presence of the characteristic hexagonal arrays of parallel carbon rods unequivocally demonstrates the successful replication of the SBA-15 used as hard template. In addition to the desired structure, small regions containing disordered carbon can also be observed in the TEM images. These species most likely find their origin in the dopant and/or carbon precursor that remained outside the SBA-15 template during the synthesis. Even after a careful fine-tuning of the amount of applied precursors to the pore volume, such species could not be completely avoided. The mesoporous structure observed by TEM is reflected by the very high specific surface area of the materials measured by means of N_2-physisorption. The structural and textural features of the doped OMC materials are summarised in Table 1. The specific surface area of POMC (1092 m^2 g^{-1}) is remarkably high among doped OMCs prepared with SBA-15 as hard template.[2,34,38] The pore size distributions of the electrocatalysts are narrow (Fig. S1†) and are centred around 3 to 4 nm (Table 1), in line with the ordered structure of materials of the OMC type.

The elemental composition of the surface layer of the different OMC materials was determined by X-ray photoelectron spectroscopy (XPS). The results confirm that the doping with B, N and P was successful, though in a different extent for each element (Table 2). Although phosphorus has the largest mismatch in size with carbon, with our specific synthesis method it was the most efficiently incorporated into the final material, followed by nitrogen and finally boron. In literature, nitrogen is generally more easily incorporated, which is to be expected based on its similar size compared to carbon.[33,51] Possibly phosphorus was more easily incorporated into the final material because the structure of its precursor (tris(4-methoxyphenyl)phosphine) more closely resembles that of graphitic carbon when compared to that of the other precursors, but also because phosphate species can form at the edge of the structure (see Scheme 2). The low doping level of boron, on the other hand, can be explained based on its preferential

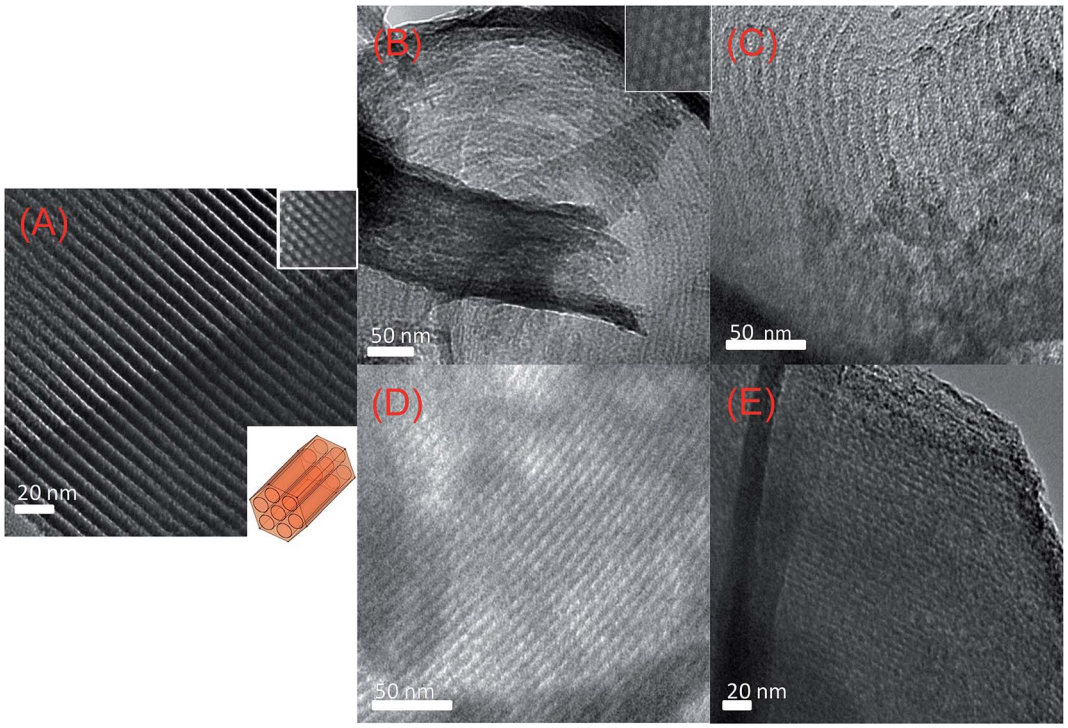

Fig. 1 TEM images of SBA-15 (A), NOMC (B), BOMC (C), POMC (D) and OMC (E). The inset of image (A & B, same scale as for the main image) shows a top view of the hexagonal array of rods. All OMC samples were measured after removing the SBA-15 template.

configuration inside the carbon framework, namely replacing a carbon atom in the sp^2 carbon lattice. Compared to nitrogen and phosphorus, which can also be incorporated at the edges or at defect sites, B incorporation is therefore bound to be more difficult.[51] Further discussion of the XPS data is provided in Section 3.2.

Based on these characterisation results, we can conclude that all the doped OMCs display the desired chemical, structural and textural features for the targeted electrocatalytic application.

3.1 Electrocatalytic performance of the doped OMCs in the reduction of nitrobenzene

Linear Sweep Voltammetry (LSV) is typically used to obtain the first ranking of different electrocatalysts in terms of activity (onset potential and generated current density) for a specific reaction, which in this case is the reduction of nitrobenzene. LSV experiments were performed in a half cell setup employing 5 mM nitrobenzene in 0.3 M $HClO_4$ in ethanol. The potential of the working electrode was varied from −0.2 to −1.8 V *vs.* Fc/Fc^+ at four different rotation speeds (500 to 2000 rpm, Fig. S2 to S5†).

The LSV results (summarised in Fig. 2 and Table 3), prove that all the OMC materials are active electrocatalysts for the reduction of nitrobenzene, thus demonstrating our starting

Table 2 Surface composition of (doped) OMCs in wt% as determined by XPS

	N (wt%)	B (wt%)	P (wt%)	C (wt%)	O (wt%)
NOMC	2.7	—	—	85	11
BOMC	0.3	1.1	—	92	5.5
POMC	0.4	—	6.2	76	18
OMC	0.1	—	—	91	8.6

Table 1 Structural and textural properties of SBA-15 and OMCs

	S_{BET}[a] ($m^2\ g^{-1}$)	Total pore volume[b] ($cm^3\ g^{-1}$)	Micropore volume[c] ($cm^3\ g^{-1}$)	Pore size[b] (nm)
SBA-15	826	0.76	0.12	7.5
NOMC	745	0.50	0.04	3.1
BOMC	848	0.89	0.03	4.0
POMC	1092	0.36	0.04	2.7
OMC	846	0.57	0.01	3.2

[a] S_{BET} is the BET surface area. [b] Total pore volume and pore size calculated with the BJH method. [c] Micropore volume determined from the *t*-plot.

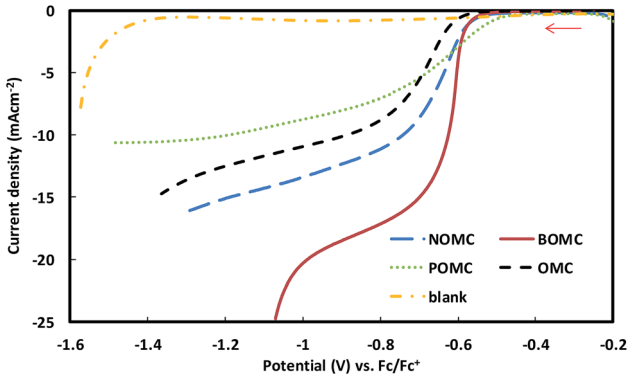

Fig. 2 LSV plots of NOMC, BOMC, POMC, OMC and blank$_{NOMC}$, recorded in 5 mM nitrobenzene and 0.3 M $HClO_4$ in ethanol at a scan rate of 5 mV s^{-1} and with a rotation speed of 2000 rpm and corrected for the *iR* drop.

hypothesis that a metal centre is not strictly needed to promote this reaction. Two main observations can be made about the four investigated electrocatalysts based on these LSV data. First of all, the electrocatalysts could be ranked in terms of onset potential, for which the least negative value was observed with POMC, followed by NOMC, OMC and finally BOMC (Table 3). Since a less negative onset potential corresponds to a lower overpotential, the reaction over the POMC involved a lower activation energy, which means that its sites are more active in initiating the reduction of nitrobenzene. On the other hand, BOMC displayed the most negative onset potential, but led to the highest current density, followed by NOMC, OMC and POMC (Table 3). This signifies that the active sites in BOMC, although less easily activated, lead to faster reaction rates, resulting in a faster reduction. NOMC and OMC display intermediate values for onset potential and current density. Finally, for all the electrocatalysts the absence of a clear plateau in the LSV curves suggests that more than one chemical is produced at the same time over this class of materials. This first set of results demonstrates that doping of OMC has a marked influence on the electrocatalytic behaviour of the materials. However, the results discussed so far do not include any information on the selectivity of the electrocatalysts. To gain information on the selectivity, Koutécky–Levich (K–L) plots were constructed based on the data from the LSV experiments performed at different rotation speeds. The Koutécky–Levich plots for the NOMC electrocatalyst are presented in Fig. 3, those for the other materials can be found in the ESI (S6 to S8†). Based on these plots, it is possible to determine n from the slope and the kinetic current density (J_K) from the intercept. The number of exchanged electrons allows a first evaluation of the selectivity of the electrocatalysts in the reduction of nitrobenzene. To have a high selectivity towards aniline, the value for n should be as close as possible to 6 (see Scheme 1). The kinetic current density is a measure of the activity of the electrocatalysts. Particularly, when comparing two electrocatalysts for which the number of exchanged electrons is the same, a higher kinetic current density is a direct indication of a higher electron transfer rate constant. The similarity of the slopes in the K–L plots (Fig. 3 and S6–S8†) indicates that the value for n remains almost constant in the investigated potential window, which implies that the selectivity of the reduction reaction does not change significantly in this potential range. The values for n, J_K, onset potential and half-wave potential are summarised in Table 3 for the electrocatalysts under investigation. The half-wave potential ($E_{1/2}$) is correlated both with the onset potential and the current density: a more positive value is the result either of a higher kinetic current density (as in the case of BOMC) or of a more positive onset potential (as in the case of POMC). The fact that $E_{1/2}$ for NOMC, BOMC and POMC are very similar is thus caused by different factors in each case. This also implies that a more balanced and detailed evaluation of the activity of these electrocatalysts can be obtained on the basis of the onset potentials and of the kinetic current densities, rather than of the half-wave potentials.

Comparing the results summarised in Table 3, it can be concluded that the best electrocatalyst that was produced in this study is NOMC, since the average number of transferred electrons ($n = 6.0$) suggests an excellent selectivity to aniline, and the activity in terms of current density is much higher compared to the other two electrocatalysts for which n is also around 6, *i.e.* POMC and OMC. BOMC reached the highest kinetic current densities but its selectivity is expected to be inferior due to the too high value of n, which suggests that aniline was partially reduced further to cyclohexylamine

Table 3 Summary of the electrocatalytic performance of the different OMC electrocatalysts. Note: the reported values are the average of at least 2 measurements. The standard deviations are SD (n) ≤ 0.3, SD (J_K) ≤ 0.7 mA cm^{-2}, SD (E_{onset}) = 0.01 V and SD ($E_{1/2}$) = 0.01 V

Electrocatalyst	n @ −0.75 V	J_K @ −0.75 V (mA cm^{-2})	Onset potential (V)	$E_{1/2}$ (V)
NOMC	6.0	−33	−0.31	−0.62
BOMC	7.5	−110	−0.39	−0.61
POMC	5.8	−9.5	−0.24	−0.62
OMC	6.0	−16	−0.37	−0.67

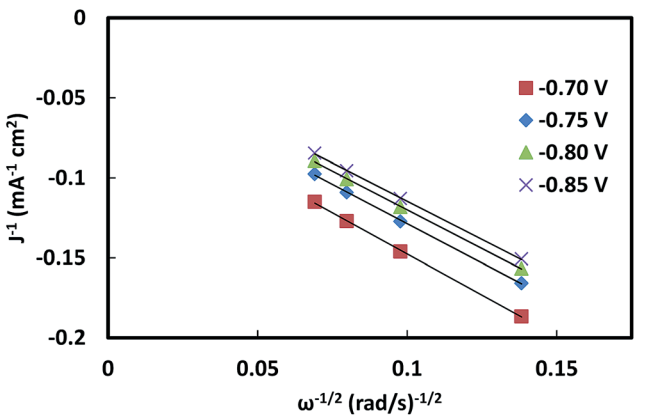

Fig. 3 Koutécky–Levich plots (J^{-1} *vs.* $\omega^{-1/2}$) of NOMC at a potential interval from −0.70 to −0.85 V *vs.* Fc/Fc^+.

(Scheme 1). It is also worth noting that OMC, which was prepared without a doping element as B, N or P, still displayed a relevant activity in the reduction of nitrobenzene.

3.2 Correlation between electrocatalytic behaviour and physicochemical properties

The physicochemical properties of the OMC materials that are expected to have a major influence on their electrocatalytic performance in the reduction of nitrobenzene are: (1) the nature of the doping element, its content and configuration, (2) the specific surface area and pore size of the material and (3) the degree of graphitisation.[34] The latter can be estimated by Raman spectroscopy, which also provides information about the amount of defects and disordered structures in the material. After deconvolution of the Raman spectra (Table 4 and Fig. 4 and S9†), four broad peaks could be distinguished: (i) a peak at 1200 cm^{-1}, attributed to aliphatic species, (ii) a peak at 1350 cm^{-1}, usually referred to as the D-band, which is correlated with defects at the edges of the graphitic domain, (iii) a peak at 1510 cm^{-1} (A-band), originating from heteroatoms or five-membered rings and, (iv) a peak at 1600 cm^{-1} (G-band), which is assigned to vibration modes of sp^2 C atoms in an ideal graphitic plane.[34] The presence of the latter is thus a clear indication of the formation of a graphitic carbon structure.[34] Compared to an ideal graphitic lattice, this peak is slightly shifted to lower wavenumbers as a consequence of the electron delocalisation caused by the incorporation of doping elements inside the carbon framework.[52] The relative degree of graphitisation can be estimated through various parameters determined from the Raman spectra: the ratio between the areas of the D and the G band (A_D/A_G) is inversely proportional to the degree of graphitisation; a lower full-width at half-maximum (FWHM) of the D-band and also a smaller area of the A-band correspond to a higher degree of order.[4,34,53] The values of these parameters for the studied OMC materials are reported in Table 4. The incorporation of boron results in the highest degree of graphitisation, and the A_D/A_G, $FWHM_{D\text{-band}}$, $A_{A\text{-band}}$ (%) values of BOMC are even lower compared to those of the OMC material, which was prepared without adding any dopant. It is inferred that the presence of boron promotes the formation of a graphitic carbon structure, in agreement with the observations reported by Choi and co-workers.[54] Moreover, the lower dopant content in BOMC compared to POMC and NOMC observed by XPS (Table 2) is also likely to have played a role in the higher graphitisation degree of BOMC. This can be understood considering that the doping elements have different size

Table 4 Summary of parameters determined by deconvolution of the Raman spectra

Sample	A_D/A_G	FWHM D-band	Area% of A-band
NOMC	1.16	141	15
BOMC	1.05	123	10
POMC	1.35	145	17
OMC	1.10	134	14

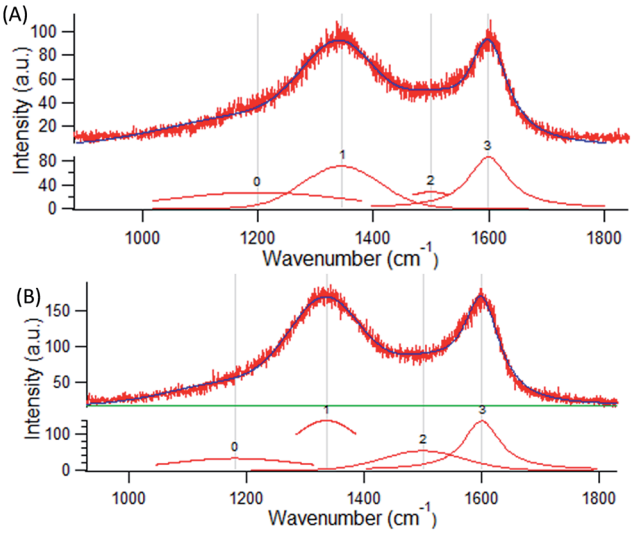

Fig. 4 Deconvoluted Raman spectra of BOMC (A) and POMC (B). The Raman spectra of NOMC and OMC can be found in Fig. S9 in the ESI.†

from C atoms and thus create defect sites. Additionally, since the difference in size between phosphorus (106 pm) and carbon (77 pm) is much larger than that between boron (82 pm) or nitrogen (75 pm) and carbon, phosphorus tends to be located slightly above the carbon framework. This results in a more distorted structure and, therefore, can account for the lowest degree of graphitisation observed for POMC (*i.e.* for the highest values for each of the parameters in Table 4).[51]

The specific surface areas of all the materials synthesised in this work are high, ranging from 745 $m^2\ g^{-1}$ for NOMC to 1092 $m^2\ g^{-1}$ for POMC (Table 1). All materials have the desired narrow pore size distribution in the mesoporous range (average pore size between 2.7 nm for POMC to 4.0 nm for BOMC – see Table 1 and Fig. 1 and S1†). These features are expected to grant a good accessibility of the active sites of the electrocatalysts. When comparing the different OMC materials, no specific correlation was found between these structural and textural properties and the electrocatalytic performances. This suggests that even the lowest specific surface area of the series (NOMC) is sufficiently high to guarantee an optimum accessibility of the active sites, and that for these OMC materials the nature of the doping elements and the graphitisation degree become the factors determining the differences in catalytic behaviour.

Characterisation by XPS did not only provide information about the loading of each doping element in BOMC, NOMC and POMC (*vide supra*) but also evidenced that all the prepared materials display a significant content of oxygen, which most likely originates from the exposure of the electrocatalysts to air during the thermal treatments. The O content varies from 5.5 wt% in BOMC up to 18 wt% in POMC (Table 2). It can be inferred that O atoms are more readily incorporated in OMCs with a lower degree of graphitisation (BOMC has the highest and POMC the lowest degree of order – see Table 4) as a consequence of the preferential incorporation of oxygen at the edges or at defect sites.[55,56] It is also worth mentioning that even

in the absence of N during the synthesis, a small fraction of N was found in BOMC, POMC and OMC (Table 2). This is most likely due to a minor contamination from previous uses in the tubes used for the pyrolysis step. No signals due to transition metals were observed by XPS. Additional elemental analysis of POMC by a technique with a lower detection limit as X-ray fluorescence (XRF), indicated that only traces of Fe, Ni and Cu were present in the material (≤0.01 wt% of each transition metal, see Table S1†). These values are significantly lower compared to the transition metal impurities found in other carbon materials used in electrocatalysis (for example, carbon nanotubes contain typically 0.1–0.5 wt% of iron[57] and 0.01 to 0.1 wt% of other transition metals[58]). These data imply that the OMCs cannot be considered as strictly metal-free materials, but the amounts of adventitious transition metals are so low that these impurities are expected to have only a minor influence, if any, on the electrocatalytic performance. This hypothesis is supported by the marked difference in activity and selectivity between the different OMCs (see Table 3) and by the role of the dopants on the electrocatalytic behaviour ascertained by DFT simulations (*vide infra*).

XPS also provides valuable information about the configuration of the different elements, which is expected to play a role in defining the electrocatalytic behaviour of the OMC materials. The configurations are obtained by deconvoluting the high resolution signals characteristic of each element (Fig. 5). The N 1s signal is generally deconvoluted into four individual peaks that are attributed to pyridinic N (≈398.7 eV), pyrrolic N (≈400.5 eV), graphitic N (≈401.9 eV) and oxidised pyridinic N (>402.8 eV).[34,51] In the NOMC material, the largest fraction of N substituted carbon in the sp^2-C plane (graphitic N, 54%), followed by pyridinic N (33%), oxidised pyridinic N (9.8%) and pyrrolic N (3.3%). The oxidised pyridinic N species likely originate from exposure to air of the pyridinic N sites. The B 1s signal of BOMC could be deconvoluted into two peaks, at 200.5 eV (39%) and at 198.5 eV (61%), which are assigned to graphitic B (or boron replacing carbon in hexagonal rings) and to B located in the conjugated π-system but at internal defects or edges (see Scheme 2).[59] The latter bear a resemblance to borabenzene, which is a strong Lewis acid. The P 2p signal of POMC was deconvoluted into two distinct peaks, one assigned to the P–C bonds (132.6 eV, 64%) and one to P–O bonds (134.9 eV, 36%), in line with the relatively high O content observed in this material. Phosphorus can be found either in the bulk of the carbon structure or at the edges, although in the latter location P is expected to be prone to oxidation.[60,61] The P–O configuration is generally attributed to oxidised P atoms that originate from exposure to air of the P sites in the carbon structure, or to $-PO(OH)_2$ functional groups (see Scheme 2).[43,60,61]

Finally, the O 1s XPS signals were deconvoluted for all the studied materials (Fig. 5 and S10 in the ESI†). In all cases, three distinct peaks were found: one for C–O species (531.5 eV), one for C═O species (532.6 eV) and a final one for O–C═O species (533.8 eV).[34] For POMC, the peak at 531.5 eV can also be due to P–O species and the peak at 532.6 eV to P═O species.[34,62] The actual presence of these P–O and P═O is strongly supported by

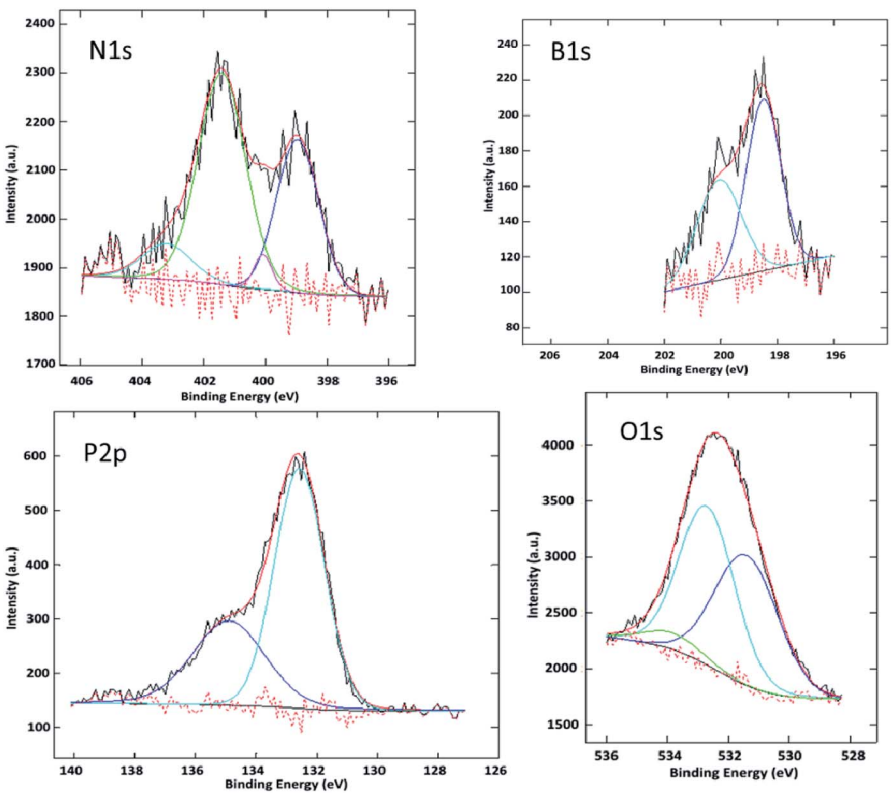

Fig. 5 Deconvoluted high resolution N 1s (NOMC), B 1s (BOMC), P 2p (POMC) and O 1s (OMC) XPS signals.

the P–O peak that was identified by deconvoluting the P 2p signal. For all materials, the C–O species make up the largest fraction, followed by C=O and O–C=O (Table 5).

The results of the detailed characterisation of the OMC materials were combined with Density Functional Theory (DFT) calculations to explain the performance of the different electrocatalysts in the reduction of nitrobenzene. The electrocatalytic activity of carbon materials doped with P, B or N is generally attributed to the local disruption of the electroneutrality of pure carbon materials.[63] The difference in electronegativity between the doping element and the neighbouring carbon atoms leads to the creation of a partial positive charge on the more electropositive element and of a partial negative charge on the more electronegative element. The positively charged sites can act as catalytic sites by interacting with nitrobenzene and thus promoting its subsequent reduction.[2,34,51] B and P are more electropositive than C, whereas N is more electronegative. On the other hand, N and P contain one more electron in the valence shell compared to C, whereas B contains one less electron than C in the valence shell. Therefore, each doping element is expected to have a distinct effect on the electrocatalytic performance of the doped OMCs. First of all, phosphorus and nitrogen significantly shift the onset potential to more positive values compared to the undoped OMC (oxygen incorporation is not considered as doping in this context). On the other hand, boron-doping generates an electrocatalyst with a higher overpotential (*i.e.* more negative onset potential). In order to explain the trend in the overpotential values, DFT calculations were performed by using a graphene layer to model the surface of the doped OMC. The effect of doping was studied by examining how the electronic structure of the graphene layer is altered by the presence of B, N and P atoms in graphitic positions. Fig. 6 compares the density of states (DOS) and the projected density of states (PDOS) of undoped graphene (top panel) with those of B-, N- or P-doped systems (from the second to the fourth panel). In pure graphene, the Fermi energy (E_F), represented by dashed line located at 0 eV, coincides with the Dirac point located at K and K' points of the first Brillouin zone of the band structure reported in Fig. S11.† In the B-doped graphene used to simulate the BOMC surface, the E_F shifts down in energy, falling into the graphene valence band. Electrons from the π-band of graphene are trapped in electronic states originating from the B atoms and appearing −0.89 eV below the Fermi level of pure graphene, as shown by the PDOS (blue curve of the second panel of Fig. 6). In contrast, when graphitic N is introduced in graphene, E_F moves up in energy and is found at +0.93 eV with respect to E_F of pure graphene. This means that N atoms donate electrons to the graphene conduction bands. Indeed, N atoms generate states close to E_F (Fig. 6, third panel), which originate from the hybridisation of nitrogen orbitals with π* states of graphene. A similar trend but with a more pronounced upward E_F shift (larger than 1 eV) was found when graphitic-like P atoms were introduced in graphene (Fig. 6, fourth panel). These DTF data confirm that B atoms in graphene act as electron acceptors (p-type dopant) whereas N and P atoms act as electron donors (n-type doping), causing the observed downwards (B-doping) or upwards (N- and P-doping) shift of E_F compared to the E_F reference level of pure graphene. The lower the Fermi level, the higher the ionisation potential of a material, thus indicating that it is easier to extract electrons from P-doped graphene, followed by N-doped graphene, pure graphene and finally B-doped graphene. These results explain the trend of the onset potential values measured experimentally (Table 3).

The trend of kinetic current density is totally different from that observed for the onset potentials: boron-doping generates active sites that lead to much higher reaction rates (higher J_K) over BOMC compared to the other OMC systems. This electrocatalytic behaviour could be explained assuming that BOMC has very active catalytic sites or the highest number of active sites but also that such sites give the highest value for the number of exchanged electrons. The latter is true ($n = 7.5$, see Table 3), but the difference compared to the other electrocatalysts is not such as to justify the remarkably higher kinetic current density observed for BOMC (Table 3). It is difficult to estimate the number and intrinsic activity of the catalytic

Table 5 Oxygen configuration of the different electrocatalysts as determined by deconvolution of the O 1s XPS spectra

	% C–O	% C=O	% O–C=O
NOMC	77	18	4.8
BOMC	59	29	12
POMC	85[a]	12[b]	3.3
OMC	76	15	5.5

[a] C–O and P–O species. [b] C=O and P=O species.

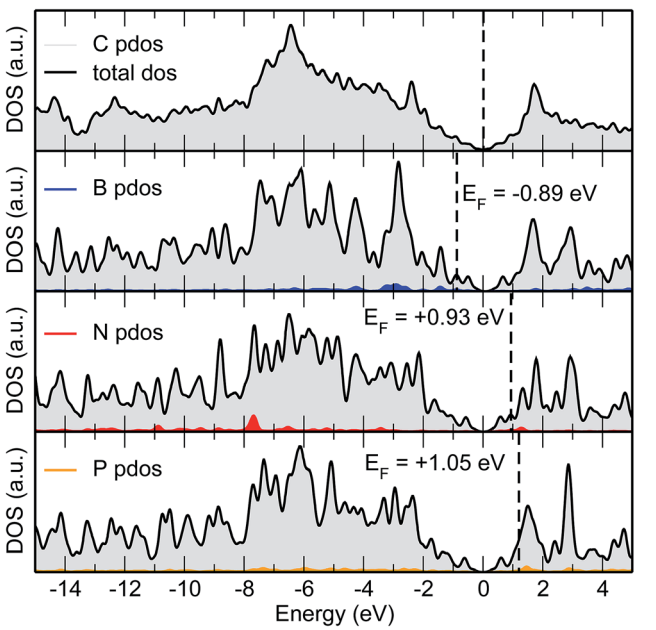

Fig. 6 Density of states (DOS) and the projected density of states (PDOS) of pure graphene (top panel) and B-, N- or P-doped graphene with the doping element in graphitic configuration (second, third and fourth panel, respectively).

sites in the doped OMC materials because the activity does not only depend on the dopant content but also on its configuration. However, the fact that BOMC displays the highest kinetic current density while having the lowest dopant content (Table 2) suggests that both configurations of B observed by XPS are highly active sites for nitrobenzene reduction. The trends in kinetic current density can be rationalised considering the difference in the partial positive charge density that is generated on B, P or C (in the case of N-doping) and taking into account that the larger is the partial positive charge, the faster the reduction is expected to proceed.[34,51] From theoretical calculations performed in the literature, the partial positive charge decreased from 0.62 on B to 0.28 on C (next to N) to 0.21 on P.[64–66] This trend is in line with the observed trends in kinetic current density (Table 3). Another factor that most likely contributed to the high J_K over BOMC is its higher graphitisation degree, proven by Raman spectroscopy. A highly graphitic material is more conductive compared to materials with a lower degree of graphitisation and, therefore, its electron transport is faster and a higher reduction rate can be achieved.[34] The second highest kinetic current density among the studied OMC electrocatalysts was observed with NOMC (Table 3). This is fully in line with the partial positive charge generated by N-doping (see above) and the degree of graphitisation of NOMC estimated by Raman spectroscopy (see Table 4), which are both characterised by intermediate values between those of BOMC and POMC. The undoped OMC displayed only moderate activity compared to BOMC and NOMC, but the observed kinetic current is actually slightly higher than that found over POMC (Table 3). This is a somewhat unexpected result because the only heteroatom in this material is oxygen, which can get incorporated in functional groups but not into the graphitic structure. Therefore, no disruption of the electroneutrality of the bulk carbon occurs (differently from the B-, N- and P-doped materials) and the activity of undoped OMC materials is typically attributed to defect and edge sites devoid of oxygen,[56] though the possibility of a contribution by some of the O-containing functional groups (*e.g.* phenol) cannot be excluded. The higher J_K found over OMC compared to POMC can be also related to the higher degree of graphitisation and thus to the higher electron conductivity of the former.[51]

Most of the studied electrocatalysts (NOMC, POMC and OMC) promoted the reduction of nitrobenzene by transferring the number of electrons that is expected for the selective formation of the desired aniline as product ($n = 6$). Only BOMC led to a higher average number of exchanged electrons ($n = 7.5$). This strongly suggests a further reduction of aniline with formation of cyclohexylamine (*vide infra*). This is most likely due to the relatively large partial positive charge generated by boron-doping, which imparts Lewis acid character to the sites, thus causing the formed aniline (a weak Lewis base) to remain adsorbed on the electrocatalyst surface and thus to undergo further reduction. A similar behaviour was also observed in the oxygen reduction reaction.[67]

3.3 Chronoamperometric study of BOMC and NOMC

The two most promising electrocatalysts identified in the LSV study, *i.e.* NOMC and BOMC, were investigated further by means of cyclic voltammetry and chronoamperometry. The former technique allowed studying another parameter that is important for the practical applicability of the electrocatalysts: the stability under operating conditions. This parameter was evaluated by comparing the current density of the second cycle (after initial stabilisation) with the 1000th cycle (Fig. 7). The rather small difference in current density after 1000 cycles indicates a good degree of stability of the electrocatalysts under the employed conditions. This is a promising feature in view of a possible application in a fuel cell for the cogeneration of aniline and electricity.

The chronoamperometric study provided very important information about the activity and selectivity of the electrocatalysts on the basis of the GC analysis of the reaction medium at the end of the experiment (Table 6). The nitrobenzene conversion achieved over NOMC (61%) is significantly higher than that over BOMC (30%) as a consequence of the lower current generated over the latter throughout the experiment. This trend is opposite to what would be expected based on the LSV study, in which higher current was generated over BOMC (Fig. 2 and Table 3). Careful control experiments confirmed the correctness of these trends. The only difference in the experimental conditions was the concentration of nitrobenzene, which was 5 mM in the LSV tests and 15 mM in the chronoamperometric study. To investigate the observed behaviour in more detail, additional LSV measurements at higher nitrobenzene concentrations (15 and 30 mM) were performed (Fig. S12†). From these plots it could be observed that the increase in current density for NOMC in the tests with higher nitrobenzene concentration is more pronounced than for BOMC. This suggests that the various steps involved in the reduction of nitrobenzene (Scheme 1) occur at different rate on each of the two electrocatalysts, which would not be surprising if we consider the rather different physicochemical features of the two materials. A difference in adsorption strength and conversion rate for each of the compounds involved in the multi-step mechanism would imply that the rate law and thus the effect of nitrobenzene concentration differ between the two electrocatalysts.[33]

The correctness of the conversion values obtained from the GC analysis was also confirmed by means of Faraday's law, which estimated the nitrobenzene conversion at 61% for NOMC and 29% for BOMC. The product distributions observed at the end of the chronoamperometric test are reported in Table 6. The difference in selectivity between NOMC and BOMC evidenced by the different n values obtained from the K–L analysis was confirmed by chronoamperometry. NOMC achieved the expected and desired high selectivity towards aniline (87%), whereas BOMC only reached a selectivity of 37% towards aniline. In accordance with its higher value for n, further reduction of aniline to cyclohexylamine was observed over BOMC (selectivity of 37%). Besides a lower selectivity to aniline, BOMC also results in a larger fraction of side-products,

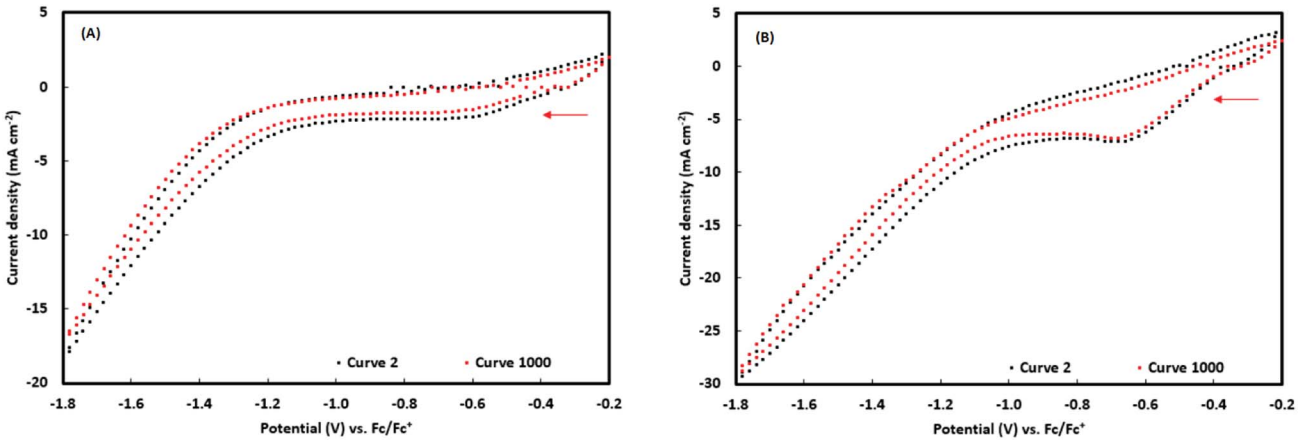

Fig. 7 Stability test of (A) NOMC and (B) BOMC by cyclic voltammetry. The potential was cycled between −0.2 and −1.8 V *vs.* Fc/Fc$^+$ at a scan rate of 100 mV s^{-1}. Only the second (after initial stabilisation) and the last curve are presented here. After 999 cycles, the measurement was paused and the solution was stirred to ensure a homogeneous nitrobenzene concentration throughout the medium. Afterwards, the last scan was measured.

Table 6 Results of GC analysis after chronoamperometric experiment performed at −0.75 V *vs.* Fc/Fc$^+$ in 15 mM nitrobenzene in 0.3 M $HClO_4$ ethanolic solution for 52 h at room temperature

	NOMC	BOMC
Conversion	61%	30%
Selectivity		
Aniline	87%	37%
Cyclohexylamine	0.0%	37%
Nitrosobenzene	3.6%	13%
Para-ethoxyaniline	5.4%	4.0%
Azobenzene	0.4%	1.0%
Azoxybenzene	3.3%	7.7%

including nitrosobenzene (two-electron reduction), azoxybenzene and *para*-ethoxyaniline. The latter two side-products are obtained through non-electrochemical conversions of the unstable intermediate phenylhydroxylamine, which cannot be detected by means of GC.[1,12,13,28,68,69]

In summary, NOMC was identified as the most promising electrocatalyst for the reduction of nitrobenzene based on the combination of its activity, selectivity and stability, which enabled to reach 61% conversion with 87% selectivity towards the desired aniline after 52 h at room temperature. Only one other doped carbon material has been reported in the literature as electrocatalyst for nitrobenzene reduction (N-doped diamond).[32] However, the comparison with the performance of our NOMC is made virtually impossible by the extremely different and much less challenging conditions used in the literature report, in which the aim was to remove nitrobenzene pollution from a solution and for which purpose much lower nitrobenzene concentration (0.81 mM *vs.* 15 mM in this work) and much higher electrode surface area (400 mm^2 *vs.* 20 mm^2) were employed. On the other hand, the performance of our NOMC can be compared to the state-of-the-art non-noble metal-containing electrocatalysts for this reaction, which were tested under analogous conditions.[1,12,33] NOMC achieved enhanced activity and a much higher selectivity towards aniline compared to Cu/Cu$_x$O nanoparticles supported on carbon nanotubes or on activated carbon. This was demonstrated both by the increased *n* value (from 4 to 6) and by the much higher aniline selectivity measured in the chronoamperometric tests. The NOMC electrocatalyst is also superior in terms of yield and selectivity towards aniline compared to the previous optimum for this reaction, *i.e.* the recently reported electrocatalyst prepared from activated carbon and polyaniline and containing highly dispersed Cu$_x$O/Cu species.[33]

With the purpose of shedding more light on the nature of the active sites of NOMC in the adsorption and subsequent reduction of nitrobenzene, we performed DFT simulations of the interaction of nitrobenzene with the surface of N-doped graphene systems in which N atoms were either in graphitic or pyridinic sites, *i.e.* the two most abundant configurations based on the XPS results (*vide supra*). In the highest occupied orbital (state at the Fermi level) of these N-doped materials, the electron density is mostly localised around the graphitic N and the pyridinic N (Fig. 8A and B). When nitrobenzene is added to the model, the lowest energy configuration is obtained if nitrobenzene lays with the aromatic ring parallel to the doped graphene plane, with the nitro group in close proximity to the N atom (either graphitic or pyridinic). In particular, the two oxygen atoms of the nitro group point towards two C atoms of graphene that are first or second neighbours of the N dopant (Fig. 8C and D). The calculated adsorption energy (ΔE_{ads}) for nitrobenzene is −0.54 eV and −0.52 eV with molecule-surface distance of 2.96 and 2.93 Å in the case of graphitic N and pyridinic N, respectively (Table S2†). These adsorption geometries are energetically more favourable compared to configurations with the aromatic ring perpendicular to the graphene plane (Fig. S13 and Table S2†). The role of N-doping is further proven by the significantly lower adsorption energy of nitrobenzene on undoped graphene (−0.38 eV). Based on these DFT results, it can be concluded that both graphitic N and

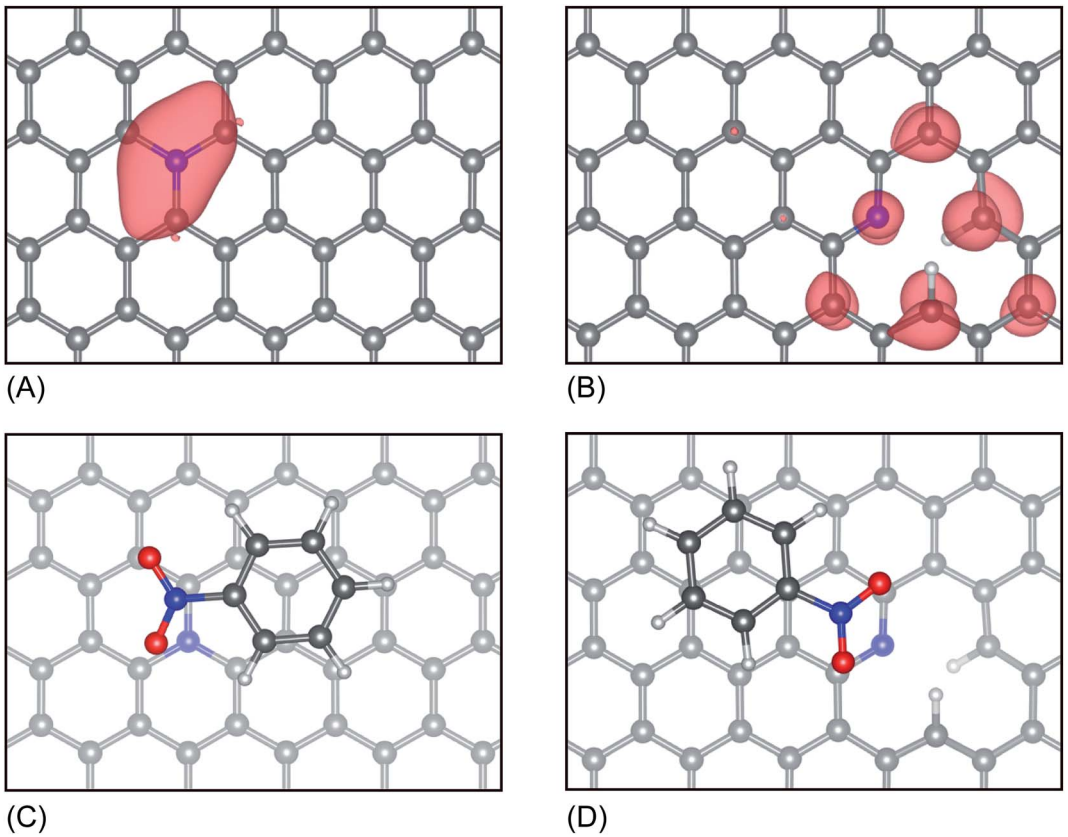

Fig. 8 Electronic density isosurfaces of the highest occupied state of N-doped graphene (used to simulate the NOMC surface) in which the N atoms are in graphitic (A) or pyridinic (B) configuration. Ball-and-stick representation of the most stable adsorption geometries of nitrobenzene on N-doped graphene in which the N atoms are in graphitic (C) or pyridinic (D) configuration [grey spheres represent C atoms, red spheres O atoms, blue spheres N atoms and white spheres H atoms].

pyridinic N atoms can generate catalytic sites for the reduction of nitrobenzene because the electrons that are more easily extracted from the electrocatalyst are spatially localised in the region around the N dopants, where the adsorption of nitrobenzene is also favoured.

Based on a preliminary estimation, the NOMC is also competitive in terms of materials cost,[70] further underlying the benefits of this virtually metal-free electrocatalyst. The high activity and selectivity towards aniline are very promising in the perspective of application of NOMC in a fuel cell for the cogeneration of this industrially relevant product and electricity.

4. Conclusions

Ordered mesoporous carbons doped with boron, nitrogen or phosphorus were synthesised, thoroughly characterised and tested as electrocatalysts for the reduction of nitrobenzene to aniline in a half-cell setup. The developed nanocasting synthesis methods using SBA-15 silica as hard template were successful in producing the targeted mesoporous materials with high specific surface area (up to 1092 $m^2\ g^{-1}$), uniform pore sizes and containing the desired doping elements. The performance of the electrocatalysts was ranked on the basis of their onset potential, kinetic current densities and number of exchanged electrons. Remarkably, the ranking of the different materials differed for each of these electrochemical parameters. Based on the onset potential, POMC emerged as the best material, while BOMC outperformed the other electrocatalysts with respect to kinetic current density. Finally, NOMC and OMC reached the highest selectivity to aniline, based on the number of exchanged electrons. DFT simulations indicated that the difference in the onset potential between the doped OMC materials can be understood in terms of the modification induced in the ionisation potential of the catalyst upon doping with different atomic species. This ultimately effects the energy required to extract electrons from the OMCs during the reduction reaction. Combining the different catalytic properties, NOMC was identified as the material with the best electrocatalytic performance in the target reaction. In a chronoamperometry test, this electrocatalyst achieved a conversion of 61% with a selectivity of 87% towards aniline after 52 h of reaction at −0.75 V *vs.* Fc/Fc^+ in 0.3 M $HClO_4$ at room temperature. This corresponds to the highest yield and selectivity towards aniline ever reported for the electrochemical reduction of nitrobenzene under comparable conditions. DFT results showed that doping with N atoms generates actives sites for promoting the adsorption and subsequent reduction of nitrobenzene.

In conclusion, NOMC was identified as a relatively affordable material with highly promising electrocatalytic performance for the perspective application in a fuel cell allowing the cogeneration of electricity and aniline as a valuable commodity product.

Conflicts of interest

There are no conflicts to declare.

Acknowledgements

The authors acknowledge sponsoring from the Flemish agency for Innovation by Science and Technology (IWT) in the frame of a PhD grant (ND). We thank Prof. Jin Won Seo and the MTM department of the KU Leuven for their support in the TEM analyses and the Flemish Hercules Stichting for its support in HER/08/25, Gina Vanbutsele (KU Leuven) for helping with the N_2 physisorption measurements and Léon Rohrbach (University of Groningen) for support with the XRF measurements.

Notes and references

1 X. Sheng, B. Wouters, T. Breugelmans, A. Hubin, I. F. J. Vankelecom and P. P. Pescarmona, *ChemElectroChem*, 2014, **1**, 1198–1210.
2 X. Sheng, N. Daems, B. Geboes, M. Kurttepeli, S. Bals, T. Breugelmans, A. Hubin, I. F. J. Vankelecom and P. P. Pescarmona, *Appl. Catal., B*, 2015, **176–177**, 212–224.
3 D. S. Su and G. Centi, *J. Energy Chem.*, 2013, **22**, 151–173.
4 N. Daems, X. Sheng, Y. Alvarez-Gallego, I. F. J. Vankelecom and P. P. Pescarmona, *Green Chem.*, 2016, **18**, 1547–1559.
5 Y. Alvarez-Gallego, X. Dominguez-Benetton, D. Pant, L. Diels, K. Vanbroekhoven, I. Genné and P. Vermeiren, *Electrochim. Acta*, 2012, **82**, 415–426.
6 W. R. P. Barros, R. M. Reis, R. S. Rocha and M. R. V. Lanza, *Electrochim. Acta*, 2013, **104**, 12–18.
7 R. M. Reis, A. A. G. F. Beati, R. S. Rocha, M. H. M. T. Assumpção, M. C. Santos, R. Bertazzoli and M. R. V. Lanza, *Ind. Eng. Chem. Res.*, 2012, **51**, 649–654.
8 E. Brillas, F. Alcaide and P. L. Cabot, *Electrochim. Acta*, 2002, **48**, 331–340.
9 M. H. M. T. Assumpção, R. F. B. De Souza, D. C. Rascio, J. C. M. Silva, M. L. Calegaro, I. Gaubeur, T. R. L. C. Paixão, P. Hammer, M. R. V. Lanza and M. C. Santos, *Carbon N Y*, 2011, **49**, 2842–2851.
10 W. Lewdorowicz, W. Tokarz, P. Piela and P. K. Wrona, *J. New Mater. Electrochem. Syst.*, 2006, **9**, 339–343.
11 K. Otsuka, H. Sawada and I. Yamanaka, *J. Electrochem. Soc.*, 1996, **143**, 3491–3497.
12 B. Wouters, X. Sheng, A. Boschin, T. Breugelman, E. Ahlberg, I. F. J. Vankelecom, P. P. Pescarmona and A. Hubin, *Electrochim. Acta*, 2013, **111**, 405–410.
13 X. Sheng, B. Wouters, T. Breugelmans, A. Hubin, I. F. J. Vankelecom and P. P. Pescarmona, *Appl. Catal., B*, 2014, **147**, 330–339.
14 Y. Chen, L. Xiong, W. Wang, X. Zhang and H. Yu, *Front. Environ. Sci. Eng.*, 2015, **9**, 897–904.
15 Y. Sang, B. Wang, Q. Wang, G. Zhao and P. Guo, *Sci. Rep.*, 2014, **4**, 6321.
16 P. S. Fernández, M. E. Martins and G. A. Camara, *Electrochim. Acta*, 2012, **66**, 180–187.
17 L. Roquet, E. M. Belgsir, J.-M. Léger and C. Lamy, *Electrochim. Acta*, 1994, **39**, 2387–2394.
18 M. Simões, S. Baranton and C. Coutanceau, *Appl. Catal., B*, 2011, **110**, 40–49.
19 A. Zalineeva, A. Serov, M. Padilla, U. Martinez, K. Artyushkova, S. Baranton, C. Coutanceau and P. Atanassov, *J. Am. Chem. Soc.*, 2014, **136**, 3937–3945.
20 M. Simões, S. Baranton and C. Coutanceau, *ChemSusChem*, 2012, **5**, 2106–2124.
21 J. Wang, Z. Yuan, R. Nie, Z. Hou and X. Zheng, *Ind. Eng. Chem. Res.*, 2010, **49**, 4664–4669.
22 X. Meng, H. Cheng, Y. Akiyama, Y. Hao, W. Qiao, Y. Yu, F. Zhao, S. I. Fujita and M. Arai, *J. Catal.*, 2009, **264**, 1–10.
23 J. W. Larsen, M. Freund, K. Y. Kim, M. Sidovar and J. L. Stuart, *Carbon N Y*, 2000, **38**, 655–661.
24 A. Furst, R. C. Berlo and S. Hooton, *Chem. Rev.*, 1965, **65**, 51–68.
25 Y. P. Sun, W. L. Xu and K. Scott, *Electrochim. Acta*, 1993, **38**, 1753–1759.
26 S. Jayabal and R. Ramaraj, *Appl. Catal., A*, 2014, **470**, 369–375.
27 J. Jiang, R. Zhai and X. Bao, *J. Alloys Compd.*, 2003, **354**, 248–258.
28 G. Kokkinidis and K. Jüttner, *Electrochim. Acta*, 1981, **26**, 971–977.
29 A. Cyr, P. Huot, J. F. Marcoux, G. Belot, E. Laviron and J. Lessard, *Electrochim. Acta*, 1989, **34**, 439–445.
30 L. Z. Huang, H. C. B. Hansen and M. J. Bjerrum, *J. Hazard. Mater.*, 2016, **306**, 175–183.
31 Z. Y. Sun, Y. F. Zhao, Y. Xie, R. T. Tao, H. Y. Zhang, C. L. Huang and Z. M. Liu, *Green Chem.*, 2010, **12**, 1007–1011.
32 Q. Zhang, Y. Liu, S. Chen, X. Quan and H. Yu, *J. Hazard. Mater.*, 2014, **265**, 185–190.
33 N. Daems, J. Wouters, K. Baert, C. Poleunis, A. Delcorte, A. Hubin, I. F. J. Vankelecom and P. P. Pescarmona, *Appl. Catal., B*, 2018, **226**, 509–522.
34 N. Daems, X. Sheng, I. F. J. Vankelecom and P. P. Pescarmona, *J. Mater. Chem. A*, 2014, **2**, 4085–4110.
35 C. M. Yang, C. Weidenthaler, B. Spliethoff, M. Mayanna and F. Schuth, *Chem. Mater.*, 2005, **17**, 355–358.
36 X. Wang, J. S. Lee, Q. Zhu, J. Liu, Y. Wang and S. Dai, *Chem. Mater.*, 2010, **22**, 2178–2180.
37 Y. Xia and R. Mokaya, *Chem. Mater.*, 2005, **17**, 1553–1560.
38 R. Liu, D. Wu, X. Feng and K. Müllen, *Angew. Chem., Int. Ed.*, 2010, **49**, 2565–2569.
39 J. Masa, W. Xia, M. Muhler and W. Schuhmann, *Angew. Chem., Int. Ed.*, 2015, **54**, 10102–10120.
40 L. Wang and M. Pumera, *Chem. Commun.*, 2014, **50**, 12662–12664.
41 J. Masa, A. Zhao, W. Xia, Z. Sun, B. Mei, M. Muhler and W. Schuhmann, *Electrochem. Commun.*, 2013, **34**, 113–116.

42 H. Shi, Y. Shen, F. He, Y. Li, A. Liu, S. Liu and Y. Zhang, *J. Mater. Chem. A*, 2014, **2**, 15704–15716.
43 D. Yang, J. Park, D. Bhattacharjya, S. Inamdar and J. Yu, *J. Am. Chem. Soc.*, 2012, **134**, 16127–16130.
44 N. Daems, T. Breugelmans, I. F. J. Vankelecom and P. P. Pescarmona, *ChemElectroChem*, 2018, **5**, 119–128.
45 P. Vermeiren, R. Leysen, H. Beckers, J. P. Moreels and a. Claes, *J. Porous Mater.*, 2008, **15**, 259–264.
46 P. Giannozzi, S. Baroni, N. Bonini, M. Calandra, R. Car, C. Cavazzoni, D. Ceresoli, G. L. Chiarotti, M. Cococcioni, I. Dabo, A. Dal Corso, S. De Gironcoli, S. Fabris, G. Fratesi, R. Gebauer, U. Gerstmann, C. Gougoussis, A. Kokalj, M. Lazzeri, L. Martin-Samos, N. Marzari, F. Mauri, R. Mazzarello, S. Paolini, A. Pasquarello, L. Paulatto, C. Sbraccia, S. Scandolo, G. Sclauzero, A. P. Seitsonen, A. Smogunov, P. Umari and R. M. Wentzcovitch, *J. Phys.: Condens. Matter*, 2009, **21**, 395502–395521.
47 J. P. Perdew, K. Burke and M. Ernzerhof, *Phys. Rev. Lett.*, 1996, **77**, 3865–3868.
48 S. Grimme, *J. Comput. Chem.*, 2006, **27**, 1787–1799.
49 V. Barone, M. Casarin, D. Forrer, M. Pavone, M. Sambi and A. Vittadini, *J. Comput. Chem.*, 2009, **30**, 934–939.
50 J. D. Pack and H. J. Monkhorst, *Phys. Rev. B: Condens. Matter Mater. Phys.*, 1977, **16**, 1748–1749.
51 J. Duan, S. Chen, M. Jaroniec and S. Z. Qiao, *ACS Catal.*, 2015, **5**, 5207–5234.
52 Z. Lin, G. Waller, Y. Liu, M. Liu and C. P. Wong, *Adv. Energy Mater.*, 2012, **2**, 884–888.
53 G. Wu, C. M. Johnston, N. H. Mack, K. Artyushkova, M. Ferrandon, M. Nelson, J. S. Lezama-Pacheco, S. D. Conradson, K. L. More, D. J. Myers and P. Zelenay, *J. Mater. Chem.*, 2011, **21**, 11392–11405.
54 C. H. Choi, S. H. Park and S. I. Woo, *ACS Nano*, 2012, **6**, 7084–7091.
55 H. Wang, T. Maiyalagan and X. Wang, *ACS Catal.*, 2012, **2**, 781–794.
56 K. Waki, R. A. Wong, H. S. Oktaviano, T. Fujio, T. Nagai, K. Kimoto and K. Yamada, *Energy Environ. Sci.*, 2014, **7**, 1950–1958.
57 Y. Li, W. Zhou, H. Wang, L. Xie, Y. Liang, F. Wei, J.-C. Idrobo, S. J. Pennycook and H. Dai, *Nat. Nanotechnol.*, 2012, **7**, 394–400.
58 L. Wang, C. H. A. Wong, B. Kherzi, R. D. Webster and M. Pumera, *ChemCatChem*, 2015, **7**, 1650–1654.
59 X. Li, L. Fan, Z. Li, K. Wang, M. Zhong, J. Wei, D. Wu and H. Zhu, *Adv. Energy Mater.*, 2012, **2**, 425–429.
60 F. Niu, L.-M. Tao, Y.-C. Deng, Q.-H. Wang and W.-G. Song, *New J. Chem.*, 2014, **38**, 2269.
61 R. Li, Z. Wei, X. Gou and W. Xu, *RSC Adv.*, 2013, **3**, 9978–9984.
62 J. Liu, H. Liu, Y. Zhang, R. Li, G. Liang, M. Gauthier and X. Sun, *Carbon N Y*, 2011, **49**, 5014–5021.
63 Y. Okamoto, *Appl. Surf. Sci.*, 2009, **256**, 335–341.
64 J. Liang, Y. Jiao, M. Jaroniec and S. Z. Qiao, *Angew. Chem., Int. Ed.*, 2012, **51**, 11496–11500.
65 H. H. Wang, H. H. Wang, Y. Chen, Y. Liu, J. Zhao, Q. Cai and X. Wang, *Appl. Surf. Sci.*, 2013, **273**, 302–309.
66 X. Kong, Q. Chen and Z. Sun, *ChemPhysChem*, 2013, **14**, 514–519.
67 Y. Jiao, Y. Zheng, M. Jaroniec and S. Z. Qiao, *J. Am. Chem. Soc.*, 2014, **136**, 4394–4403.
68 A. R. Becker and L. A. Sternson, *Proc. Natl. Acad. Sci. U. S. A.*, 1981, **78**, 2003–2007.
69 D. Groskova, M. Stolcova and M. Hronec, *Catal. Lett.*, 2000, **69**, 113–116.
70 The electrocatalyst cost was calculated based on the amount of chemicals that is necessary to obtain 1 g of NOMC and Cu-PANI-AC-A, respectively, and the price of the chemicals, which was acquired from the website of Sigma Aldrich on 28-02-2018.